J. Fluid Mech. (2024), *vol*. 984, A42, doi:10.1017/jfm.2024.201

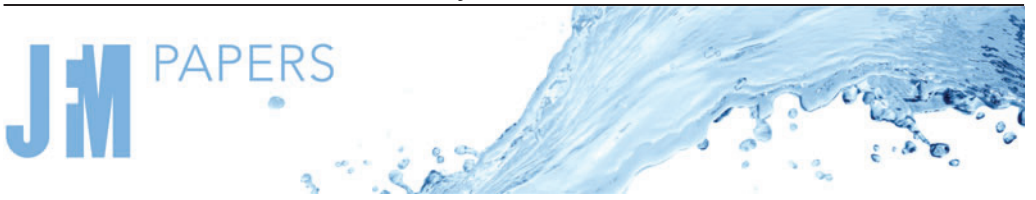

Laboratory experiments of melting ice in warm salt-stratified environments

James K. Sweetman[1,2,†], Callum J. Shakespeare[1,2], Kial D. Stewart[1,2] and Craig D. McConnochie[3]

[1]Research School of Earth Sciences, Australian National University, Canberra, Australia

[2]ARC Centre of Excellence for Climate Extremes, Canberra, Australia

[3]Department of Civil and Natural Resources Engineering, University of Canterbury, Christchurch, New Zealand

(Received 6 October 2023; revised 1 January 2024; accepted 19 February 2024)

Melting icebergs provide nearly half of the total freshwater flux from ice shelves to the ocean, but the availability of accurate, data-constrained melting rate parametrisations limits the correct representation of this process in ocean models. Here, we investigate the melting of a vertical ice face in a warm, salt-stratified environment in a laboratory setting. Observations of the depth-dependent melting rates m and boundary layer flow speed U are reported for a range of initially uniform far-field ambient temperatures T_a above 10 °C. Ice scallops are characteristic features observed in all experiments, with the width of the scallops consistent with the theory of double-diffusive layers. The morphology of the scallops changes from symmetric about the scallop centre in the colder experiments to asymmetric in the warmer experiments. Observed melting rates are consistent with a melting rate scaling of the form $m \propto U\,\Delta T_a$ proposed by previous work in less extreme parameter regimes, where ΔT_a is the magnitude of thermal driving between the ambient and ice–fluid interface. Our results indicate that ice scalloping is closely linked to the naturally convecting flow of the ambient fluid. Depth-averaged melting rates depend on the buoyancy frequency in the ambient fluid, and double-diffusive convection promotes a turbulent-flux regime distinct from that explained previously in an unstratified regime. These findings have implications for parametrising melting rates of icebergs and glaciers in numerical models or potential freshwater harvesting operations, and provide insights into the interplay between stratification and ice melting.

Key words: double diffusive convection, ice sheets, solidification/melting

† Email address for correspondence: james.sweetman@anu.edu.au

1. Introduction

Marine terminating ice shelves found in polar regions are a vital component of Earth's climate system. The ice ablation rate, commonly called the melting rate, is determined by the magnitude of heat and solute fluxes across the ice–fluid boundary (Hewitt 2020). Dynamics in the liquid phase induces convective heat and salt fluxes, leading to non-uniform melting rates in both time and space. This effect is due primarily to the introduction of turbulent fluxes and skin friction from the convection of the meltwater plume and the naturally convecting boundary layer (Jenkins 2011). Accurate representations of the melting rates and their associated magnitudes are paramount in ocean and climate modelling (Alley *et al.* 2005).

Marine terminating ice shelves lose mass through two main processes: direct sub-surface ablation and calving at the shelf front. Calved icebergs, in particular, represent nearly half of the freshwater flux from ice shelves into the ocean (Cenedese & Straneo 2023). Once separated from the glaciers, icebergs may drift in ocean currents and veer by storm systems and topographic steering into warmer environments where their melting rate accelerates. The eventual decay of an iceberg is driven primarily by submarine processes, including wave erosion, basal melting and buoyant vertical convection (Bigg *et al.* 1997; Hester *et al.* 2021). Of these, it is generally accepted that the weakest process is buoyant vertical convection (Cenedese & Straneo 2023), which comprises both the natural convection of the ambient fluid and the resultant meltwater plume from the sides of an iceberg. In many parametrisations for iceberg decay, melting due to buoyant vertical convection is cast as a depth-averaged melting rate that has dependence only on the thermal driving ΔT_a between the ambient fluid T_a and ice–fluid interface T_i. The most common parametrisation is a power-law scaling (Neshyba & Josberger 1980; Josberger & Martin 1981; Johnson & Mollendorf 1984; Dutton & Sharan 1988; Kerr & McConnochie 2015); however, polynomial representations also appear (Neshyba & Josberger 1980; Cenedese & Straneo 2023).

One of the challenges associated with parametrising natural buoyant convection is including the influence and effects of ambient stratification. The keel depth of many icebergs can range between 100 and 400 m, meaning that their penetration into the stratified water column below the mixed layer may be non-negligible (Dowdeswell & Bamber 2007). However, there is limited knowledge of how a stratification ultimately affects the melting rate beyond the leading-order depth-dependent driving terms (i.e. thermal or haline) and idealised predictions from plume theory (Hewitt 2020).

In the laboratory experiments of McConnochie & Kerr (2016), a vertical salinity gradient was shown to induce a depth dependency to the melting rate. Their results, albeit at conditions of weak thermal driving, highlighted that commonly used unstratified melting rate scalings become increasingly inaccurate as the natural buoyancy frequency increases. The experiments of Johnson & Mollendorf (1984) demonstrated further that unstratified ambient fluids with salt concentrations typical of seawater would also exhibit higher melting rates when compared to freshwater up to a thermal driving temperature approximately 15 °C. A natural question for numerical models that intend to represent iceberg meltwater fluxes (e.g. Stern, Adcroft & Sergienko 2019) is to what extent melting rates at high thermal driving depend on salt stratification in the water column. Currently, the most utilised power-law formulation posed by Neshyba & Josberger (1980) is independent of stratification, contrary to recent evidence (McConnochie & Kerr 2016; Yang *et al.* 2023). Furthermore, the influence of morphological features due to the salt stratification, such as ice scalloping (e.g. Huppert & Turner 1980), on the average melting rate is poorly understood. Only recently, efforts with high-resolution simulations

(Wilson *et al.* 2023; Yang *et al.* 2023) have begun to elucidate the complicated nature of the problem. Parametrisations that adopt the current power-law scaling are likely to perform poorly if an iceberg drifts (or is moved intentionally; Karimidastenaei *et al.* 2021) or a glacier terminates (cf. Schild *et al.* 2018) into sufficiently warm waters where thermal driving is significant, stratification weakens, or knowledge of depth-wise melting is required.

Previous work on depth-dependent melting, focused primarily on unstratified environments, has determined that the key factor setting the fluxes to the ice is the dominant flow regime, laminar or turbulent, and the respective turbulent-flux regime: buoyancy-controlled or shear-controlled (Malyarenko *et al.* (2020) and references therein). Ultimately, heat and solute fluxes from the fluid are transferred via diffusion to the ice through a thin molecular boundary layer of thickness δ, where the fluxes are inversely proportional to δ. Considering only vertical ice faces, laminar convection predicts that δ will grow monotonically per unit distance alongslope until convective instability occurs and is followed by turbulent convection. After the transition to turbulence, δ is suppressed and modulated through eddy kinetic energy and shearing forces generated in an outer turbulent boundary layer, depending on the dominant turbulent-flux regime (Wells & Worster 2008). The buoyancy-controlled regime is typically attributed to naturally convecting systems where buoyancy provides a mechanism for turbulent production, with δ scaling with the global Rayleigh number and the fluxes scaling with the third root of the flow buoyancy, $b^{1/3}$. The shear-controlled regime is assumed to be produced from externally forced flows (e.g. tides) or when a buoyant convection flow transitions to shear-controlled if a critical Rayleigh number is exceeded (Kerr & McConnochie 2015), with δ scaling with the Reynolds number, and the fluxes scaling with the free-stream flow speed. The corollary of these flux regimes is that the local melting rate is also controlled through local buoyancy and free-stream flow speed. For melting ice in unstratified fluids, solutions to the turbulent-flux regimes through self-similar turbulent theory predict a depth-dependent power-law profile, where melting increases with distance from the flow origin (Josberger 1979). However, in the more geophysically relevant case of melting into stratified fluids, the depth-dependent solutions are non-trivial and must be solved numerically (e.g. Magorrian & Wells 2016).

In certain salt-stratification conditions, the formation of thermohaline staircases and circulation cells via double-diffusive convection has been shown to play a role in regulating melting rates (Stephenson *et al.* 2011; Rosevear, Gayen & Galton-Fenzi 2021; Wilson *et al.* 2023). The seminal laboratory study by Huppert & Turner (1980) (HT80) demonstrated that for vertical ice melting into a salinity gradient, thermohaline staircases (hereafter, layers) form with thicknesses proportional to the depth-averaged density difference between the ambient fluid and its respective isohaline freezing density, and inversely proportional to the ambient fluid's density gradient. The presence of these layers was shown to characterise the spatial structure of the melting rates as the ice face became arranged into a scalloping pattern, with the troughs (peaks) of each scallop coinciding with the core (boundary) of a layer. Although the exact melting rates within each layer were not reported, the scalloping patterns were of a profile that suggests a flow-dependent melting rate, where buoyancy is gained through fluxes to the ice, and lost through vertical displacement in a salt stratification (cf. Baines 2002). Similar scalloping patterns of ice have also been shown to manifest from flow-dependent processes unrelated to double-diffusion. Small-scale scallops (1–20 cm), common to many icebergs and ice shelves, have been observed to be created by trapped eddies generated from forced convection flows (Josberger & Martin 1981; Bushuk *et al.* 2019) and also by a density

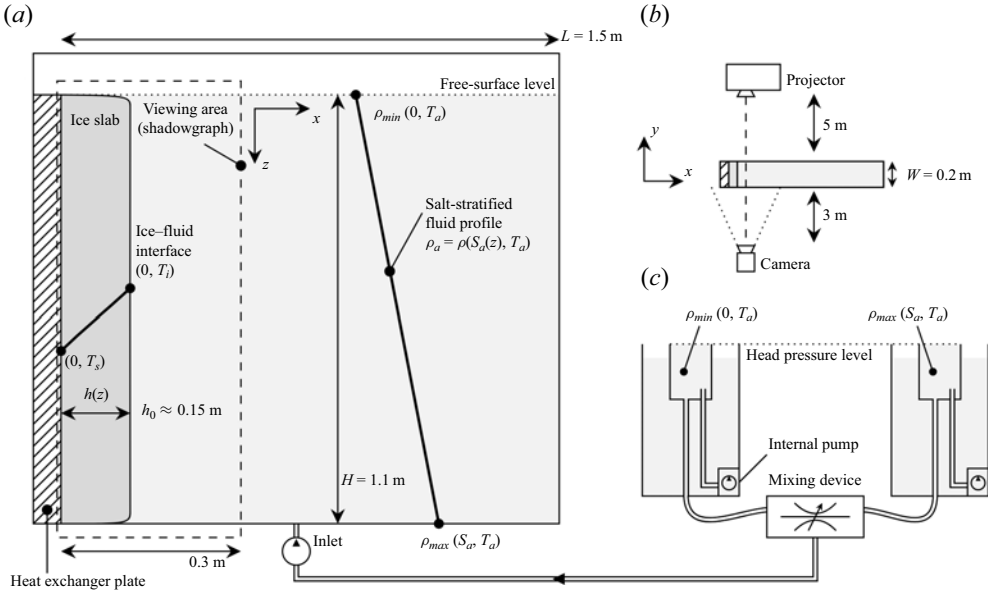

Figure 1. Schematic of the experimental set-up: (*a*) the experiment tank and its components in an observer reference frame at the initiation time of an experiment (ice-shape is rounded for added emphasis); (*b*) top-down view; and (*c*) modified 'double-bucket' system (not to scale). The coordinates (x, z, y) denote the positive horizontal, vertical and lateral directions for length, depth and width. Tank measurements (L, H, W) represent spanwise length, height and width, respectively. Temperatures T, salinities S and densities ρ are indexed by their respective feature: s, i, a for solid, interface and ambient, respectively. Ice thickness $h(z, t)$ is measured normal to the sidewall at $x = 0$ m, beginning with an initial thickness $h_0(z)$.

reversal (Weady *et al.* 2022). While the forcing mechanism differs, in both cases, the circulation structure in the ambient fluid regulates the heat, salt and volume fluxes to the ice, and therefore controls the local melting rate.

The studies cited above raise the critical question of what flux scaling law best describes the melting rate in stratified environments with active double-diffusive convection. Here, we explore this question by investigating the influence of (relatively weak) salt stratification on the local and depth-averaged melting rates through a series of laboratory experiments at conditions of high thermal driving ($\Delta T_a > 10$ K) with initially uniform far-field temperatures, a regime that previously has not been investigated experimentally (McCutchan & Johnson 2022). In § 2, we outline the experimental set-up and data collection methodology. We describe our results and evaluate the validity of existing parametrisations in § 3. A discussion of the results follows in § 4, and we conclude in § 5.

2. Methods

2.1. *Apparatus and set-up*

The apparatus shown in figure 1(*a*) consisted of a tank constructed out of double-glazed Perspex and reinforced with steel square beams, measuring 1.5 m × 1.1 m × 0.2 m ($\hat{x}$, $\hat{z}$ and $\hat{y}$ directions, respectively) housed in a constant-temperature room within the Climate and Fluid Physics laboratory at the Australian National University (cf. Kerr & McConnochie 2015). The double-glazed panes were filled with argon gas to reduce the moisture content and prevent condensation. The tank width (0.2 m) is sufficient to accommodate three-dimensional turbulence at small scales and the expected large-scale

two-dimensional double-diffusive convection cells and ice morphology (cf. Yang *et al.* 2023), as well as meaning that viscous boundary effects and any sidewall heat fluxes may be neglected safely. Within the tank, a 1.5 m $\times$ 0.2 m ($\hat{z}$ and $\hat{y}$) heat exchanger plate connected to a Julabo FP50-HD refrigerated circulator was placed along one of the sidewalls and used to grow and sustain a slab of ice at temperatures $T_s \approx -20\,^{\circ}\mathrm{C}$.

Creation of a salt-stratified fluid in the tank was accomplished by pumping mixed fluid into the base of the tank through the use of a modified 'double-bucket' arrangement composed of two 200 l drums, constant head pressure outlets, a SmartMotor-controlled mixing valve, and a pump (figure 1*c*). Usage of the modified double-bucket technique was necessary as overhead space was limited, meaning that a gravity-fed injection was not feasible. The constant pressure heads and pump maintain a constant flow rate, while the mixing valve ensures the correct ratio of 'salty' and 'fresh' throughout the fill via a Labview control program. For each experiment, the drums were preheated to the desired ambient temperature T_a, and preset with the desired salt concentration to fix the upper (ρ_{min}) and lower bounds (ρ_{max}) of the stratified fluid (refer to figure 1*a*). A viewing area spanning the full depth of the tank and 0.25 m in width was covered with shadowgraph paper and illuminated with white light by a projector located 5 m behind the tank (virtual distance). Images of this area were taken on a high-speed/resolution Basler camera positioned 3 m in front of the tank (figure 1*b*) operating at variable time intervals 500 ms (for a duration up to 1 h) and 1 min with a calibrated spatial resolution of approximately 0.3 mm.

Experiments were carried out by initially growing pure ice in the tank from freshwater (air bubbles in the ice were prevented by using an air stone to drive a continuous flow along the ice surface during solidification) until the x-wise initial thickness of the ice was $h_0 \approx 0.15$ m (10 % of experiment tank thickness). As the ice is grown *in situ*, the horizontal temperature profile within the ice is expected to span the prescribed temperature T_s at the heat exchanger and the interface temperature T_i prescribed by the equilibrium condition at the ice–fluid interface (i.e. the liquidus curve) through a constant temperature gradient. As such, colder heat exchanger temperatures imply that more sensible heat must be delivered to the ice to heat up and melt the ice, but this is a relatively modest effect. Using the Stefan number $St = c_s(T_i - T_s)/\mathcal{L}$, where $c_s \approx 2000\ \mathrm{J\ kg^{-1}\ K^{-1}}$ is the specific heat capacity of ice, and $\mathcal{L} = 3.35 \times 10^5\ \mathrm{J\ kg^{-1}}$ is the latent heat of fusion, we estimate that our configuration (with $T_s = -20\,^{\circ}\mathrm{C}$) requires approximately an extra 11 % of energy for the same melting rate as compared to previous studies where $T_s \approx -1\,^{\circ}\mathrm{C}$ (refer to McCutchan & Johnson 2022). The room temperature was then adjusted to match T_a, and the ice was partitioned off from the freshwater within the tank with a removable barrier slotted flush with the ice face. The remaining freshwater was then preheated to T_a followed by the injection of the salt-stratified fluid from the bottom of the tank, with the freshwater overflowing (to the drain) out the top. Typical injection durations were approximately 1.5 h, and due to the temperature differential, some premature melting was observed due to conduction through the barrier during this time. On average, premature melting resulted in a change in h_0 between 1 mm (coldest) and 10 mm (warmest) experiments; this premature melting is not included in our reported results. Upon creating the desired salt-stratified environment, the barrier was removed carefully ($\approx$2 min) to minimise disturbance to the stratification, and the system's evolution was recorded for up to 12 h. We note that a short-lived disturbance to the entire fluid was generated during the removal of the barrier, resulting in a barotropic sloshing motion that would persist for approximately 5 min. We also report that throughout the course of an experiment, regardless of the room temperature, there was no evidence of significant sidewall melting.

In other reference experiments with a non-salt-stratified fluid, a procedure similar to that described above was followed except for the double-bucket technique, which was replaced by direct replenishment of fluid at T_a into the experiment tank. To maintain a homogeneous ambient temperature profile and prevent the pooling of densified ambient fluid at the bottom of the tank, ultimately causing the development of a strong thermal stratification, a diffusing screen and a mixing reservoir similar to that detailed in Josberger & Martin (1981) were implemented. Further details of this unstratified configuration are given in § A.2.

2.2. *Measurements: stratification, thermal driving, and ice melting rate*

Measurements of the ambient fluid density were taken with a DMA-15 densimeter during (automated via an in-line connection) and immediately after injection into the tank (via sampling tubes), with density profiles found to be linear before removal of the barrier. The salinity profile in each experiment was inferred from the measured density profile through a realistic equation of state (Roquet *et al.* 2015). We define the initial buoyancy frequency as

$$N^2 = \frac{g}{\rho_0}\frac{\partial \rho_a}{\partial z}, \tag{2.1}$$

where the reference density is $\rho_0 = 999.8\ \mathrm{kg\ m^{-3}}$, and g is the acceleration due to gravity. The buoyancy frequency was calculated from a linear regression of the measured density gradient. Except for the non-salt-stratified cases, N is assumed to be characterised by the salinity gradient. Thermal driving is defined as $\Delta T_a = T_a - T_i$, where T_a is the initial ambient temperature (assumed constant throughout the tank), and T_i is the mean interface temperature, which may be approximated as the liquidus temperature T_L for an isohaline transformation of the ambient fluid (Vancoppenolle *et al.* 2019):

$$T_i = T_L(\bar{S}_a). \tag{2.2}$$

For all our experiments, $T_i \gtrapprox -0.54\,^{\circ}\mathrm{C}$, but hereafter we will assume $T_i = 0\,^{\circ}\mathrm{C}$ in the interests of brevity. Small variations in T_i due to salt concentrations are unimportant in the high-temperature regimes of these experiments, and an uncertainty of $\pm 1\,^{\circ}\mathrm{C}$ is assumed for T_a in all experiments, which is the variability in the room temperature control. We note that since our apparatus does not have an opposing heat exchanger to maintain the constant temperature in the ambient fluid, there is an inherent time limit to each experiment owing to the finite size of the tank before T_a changes appreciably. An estimate for this time (τ_0) can be sourced from the lateral growth rate of the layers (Malki-Epshtein, Phillips & Huppert 2004) and is considered when calculating the average melting rate.

Measurements of ice thickness were obtained by analysis of the shadowgraph images. The morphological changes to the ice–fluid interface were tracked spatiotemporally through a pipeline of filtering and edge-detection techniques (Kerr & McConnochie 2015), with the ice thickness relative to the sidewall denoted by $h(z, t)$. Applying this algorithm to the time series of images and taking the time derivative returned measurements of the instantaneous melting rate $m(z, t) = -\partial h(z, t)/\partial t$.

2.3. *Measurements: fluid velocity and boundary layer*

The fluid's time-averaged horizontal and vertical velocity components were measured by tracking flow features in the captured shadowgraph images (figure 2). Such measurements were made possible due to light intensity $I(x, z, t)$ variations arising from curvature

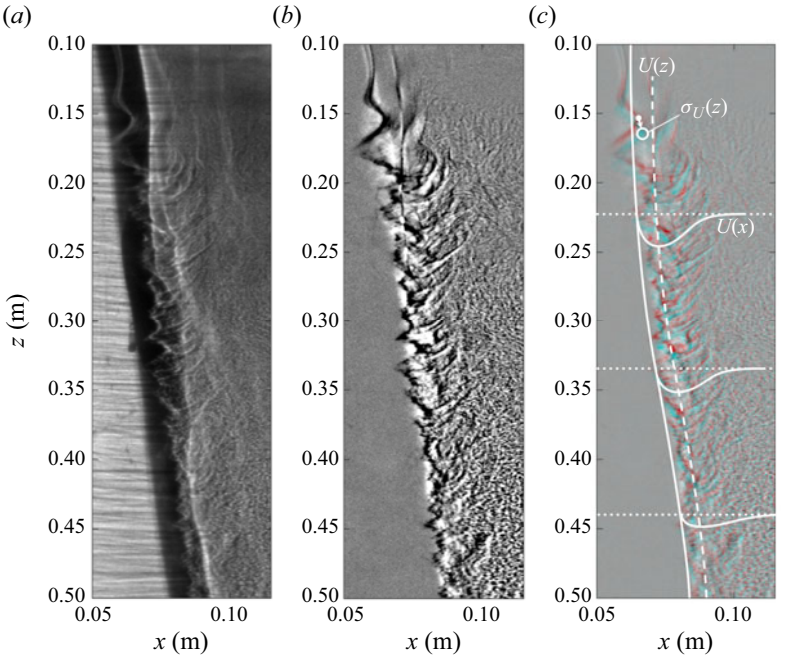

Figure 2. A close-up image of the ice–fluid interface ($T_a = 30\,^{\circ}$C). (*a*) The shadowgraph image, as captured by the camera. Some residual dye in the fluid can be seen at upper right. (*b*) The transient light field (a proxy for $\nabla^2\rho$), extracted from a subtraction of the shadowgraph image (*a*) and a rolling time average. This field's various features (e.g. filaments and turbulence) were used to measure fluid velocities. (*c*) False-colour composite of two transient images in the time series ($\Delta t \approx 500$ ms, blue–red colour denotes a feature change between images) with examples of the horizontal boundary layer velocity $U(x)$, our definition of the vertical flow speed $U(z)$, a filament being tracked, and its error window σ_U.

in fluid densities ($\nabla^2\rho$) inducing optical caustics on the shadowgraph. To improve the measurement and fidelity of the flow speeds, especially at conditions of lower thermal driving, image time series were converted into transient light intensity fields by subtracting a rolling time mean (background) field of 5 image frames before analysis (figures 2*a*,*b*). Since fluxes to the ice are moderated through the boundary layer, particularly via shear stresses, we focus on measuring its flow speed. The boundary layer is assumed to be composed of a wall-bounded meltwater plume of thickness δ_m adjacent to the ice, and an ambient fluid plume component outside of it, extending into the far field of thickness δ_a (cf. Yang *et al.* 2023) where the horizontal velocity is zero at the interface and the outer edge of the ambient layer (Carey & Gebhart 1982; Wells & Worster 2011). Because the meltwater component has the potential to be positively or negatively buoyant with respect to the ambient component (discussed in § 2.4) and the salt stratification could also affect the flow, the horizontal profile of the boundary layer is not easily generalisable since it is not necessarily constant throughout the entire fluid column. As such, we have simplified the task by considering only the maximum vertical velocity of the horizontal profile throughout the fluid column as the characteristic boundary layer flow speed (figure 2*c*).

We further restrict the region of interest to be between the ice–fluid interface and the maximum effective width of the plume, approximately 4 cm into the fluid (in the $\hat{x}$ direction). Optical features (see figure 2*b*) were tracked within this region until either substantial dissipation of the feature or significant departure from the region occurred.

T_a (°C)	10 ± 2	15 ± 2	20 ± 2	25 ± 2	30 ± 2
$\partial S_a/\partial z$ (‰ m^{-1})	7.9	8.0	8.3	6.9	4.3
$\bar{S}_a$ (‰)	3.6	3.6	3.8	3.1	2
$\partial \rho_a/\partial z$ (kg m^{-4})	6.6 ± 0.04	6.6 ± 0.01	6.3 ± 0.02	5.1 ± 0.02	3.3 ± 0.01
N (rad s^{-1})	0.2545	0.2545	0.2486	0.2237	0.1799
$\rho_{a,0}$ (kg m$^{-3)}$	1001.2 ± 0.1	999.9 ± 0.1	998.6 ± 0.1	998.0 ± 0.1	998.1 ± 0.1
A_0 (m^2)	0.102	0.152	0.154	0.134	0.122
τ (h)	9.27	3.55	2.12	1.15	0.74
$\langle \bar{m} \rangle$ ($\times 10^{-5}$ m s^{-1})	0.13 ± 0.08	0.51 ± 0.23	0.80 ± 0.27	1.29 ± 0.09	1.90 ± 0.32
$\bar{\eta}_{HT80}$ ($\times 10^{-3}$ m)	31 ± 6	96 ± 9	199 ± 18	400 ± 36	899 ± 82
$\bar{\eta}$ ($\times 10^{-3}$ m)	49 ± 26	132 ± 45	184 ± 70	288 ± 65	907 ± 3
No. of layers (count)	20	7	4	2	1
$\bar{\eta}/\bar{\eta}_{HT80}$	1.59 ± 0.91	1.38 ± 0.48	0.92 ± 0.36	0.72 ± 0.18	1.01 ± 0.09
$Ra_{\bar{\eta}}$	10^8	3×10^9	7×10^9	3×10^{10}	8×10^{11}
Ra_H	6×10^{10}	2×10^{11}	3×10^{11}	6×10^{11}	9×10^{11}
$\langle \overline{Nu}_H \rangle$	115	254	293	351	460
$\langle \bar{U} \rangle$ ($\times 10^{-3}$ m s^{-1})	1.5 ± 1.1	1.8 ± 1.0	2.5 ± 1.4	11.6 ± 4.7	15.2 ± 4.3

Table 1. List of experimental parameters for the primary set of five salt-stratified experiments and key results. Uncertainty for N is ± 0.001 rad s^{-1}. Observed initial cross-sectional area of ice A_0, characteristic melting times τ, depth-averaged melting rates $\bar{m}$, depth-averaged stratification length scales $\bar{\eta}$ following HT80 and observed depth-averaged layer thickness $\bar{\eta}$ and their ratio, as well as the number of layers. The thermal Rayleigh number evaluated at the stratification length scale $Ra_{\bar{\eta}}$ (3.2) using observed values and the global thermal Rayleigh number Ra_H, depth-averaged Nusselt number $\overline{Nu}_H$ (3.8), and depth-averaged boundary layer flow speed $\bar{U}$. Variables enclosed by angled brackets denote time-averaged values across $0 \leq t \leq \tau$.

Outside this region, the flow is assumed to not contribute to the fluxes needed for melting. This procedure was carried out over many sequences of images spanning the available time series to develop a complete picture of the boundary layer flow speed over time and depth. Instantaneous uncertainties were defined by an error window σ_U about each measurement based on probable flow trajectories inferred from neighbouring flow features, representative of both the systematic (e.g. chaotic motion) and random (e.g. feature distortions) error (see figure 2*c*). In addition, we used an Optical Flow package (Liu & Salazar 2021) to assist in identifying the unidirectional and bidirectional flow regimes as well as provide a qualitative view of the flow field (discussed in § A.3). We restricted the implementation of this technique to these insights chiefly due to inconsistencies in the calculated velocity magnitudes that occurred in the presence of vigorous turbulence.

2.4. *Parameter space and expected flow dynamics*

A total of 11 experiments were conducted, two of which were non-salt-stratified, at five different temperatures spanning 10 °C to 30 °C (see table 1). We emphasise that our parameter space is notably different from that found in the ocean, especially in density space where the ambient fluid density is comparable to that of meltwater, significantly influencing the dynamics that we observe. The meltwater from pure ice may be assumed to be ejected at close to the reference density in conditions of high thermal driving, and has buoyancy $b_m \propto \rho_a - \rho_0$. By contrast, the ambient fluid plume is always expected to cool and gain a buoyancy $b_a \propto \rho_a - \rho(S_a, T_i)$ that, given the appropriate temperature and salinity conditions, downwells when the thermal expansion coefficient $\alpha(S, T)$ is positive. Comparing the relative contributions of each plume when $\alpha > 0$ indicates that $b_m/b_a < 0$ results in a downwelling unidirectional flow, whereas $b_m/b_a > 0$ results in

bidirectional flow with meltwater upwelling. For our parameter space, this implies that meltwater can change between upwelling ($\rho_0 < \rho_a$) or downwelling ($\rho_0 > \rho_a$) depending on the temperature and salinity of the ambient fluid, and because the salinity field is also a function of depth, also exhibit both flow states throughout the fluid column. These facts mean ultimately that various flow regimes in the boundary layer spanning the unidirectional upwelling and downwelling cases are possible, depending on the ambient conditions. For unstratified environments, the mapping for the resultant boundary layers is known from Carey & Gebhart (1982). Based on their work, we generally expect the dominant contributor of the boundary layer flow to transition from a bidirectional but mostly upwelling meltwater plume at cold temperatures, to a mostly downwelling ambient fluid plume at $T_a \approx 20\,^{\circ}\mathrm{C}$ as the ambient temperature is increased. However, we also anticipate the salt stratification impeding the flow regimes and being influenced by double-diffusive convection as described by HT80. We note for clarity that the unidirectional downwelling dynamics are not representative of typical ocean salinities ($\approx$35 ‰), as meltwater is significantly more buoyant relative to the ambient fluid and will generally dominate the boundary layer flow.

3. Results

Here, we focus on a primary set of five experiments with similar salt stratifications and reference salinities of approximately 0 ‰, but with varying thermal driving. Additional experiments with different salt and thermal stratification and reference salinities are described in § A.1. Uncertainties in the results that follow are all given at one standard deviation. We begin with a synopsis of the characteristic ice melting behaviour and overall flow dynamics, followed by quantitative analyses of the layering, melting rates and boundary layer flow speed.

3.1. *Qualitative observations*

In all experiments, ice was observed to melt from a planar state of near-constant thickness h_0 and rapidly morph into distinct ice scallops. Figure 3(*a*) shows example snapshots of the ice face from each experiment at a time when scallops are well established. The morphological evolution of the ice face, as shown in figure 3(*b*) in terms of the ratio of ice melted, demonstrates that once formed, scallop positions and peak-to-peak distances (hereafter, scallop wavelength) are mostly constant for the duration of the experiment. As inferred from the consistent shape of ice thickness contours in figure 3(*b*), the scallop wavelengths appear to be near constant within each case, but growing as a function of thermal driving. This observation is generally consistent with the ice scallops observed by HT80, with scallop wavelengths appearing to follow the characteristic stratification length scale scaling $\bar{\eta}$ predicted therein (see § 3.2). However, as T_a increases, the scallop profiles observed in our experiments change between experiments from symmetrically concave shapes to asymmetrical sawtooth-like shapes (the sawtooth shape is exemplified in figure 3*b* iv). We note that this kind of scalloping is dissimilar to that reported in Bushuk *et al.* (2019) and Weady *et al.* (2022), which has wavelengths on the O(5 cm) scale and manifests from self-reinforcing eddies trapped between the boundary layer flow and ice–fluid interface, but is broadly consistent with the observations of Yang *et al.* (2023). The lack of smaller-scale scalloping features in our experiments suggests that the flow dynamics influenced by the density extremum (cf. Weady *et al.* 2022) are irrelevant in the present experiments. We remark that no evidence for significant spanwise variations in the melting of ice, as well as small-scale three-dimensional turbulent melting

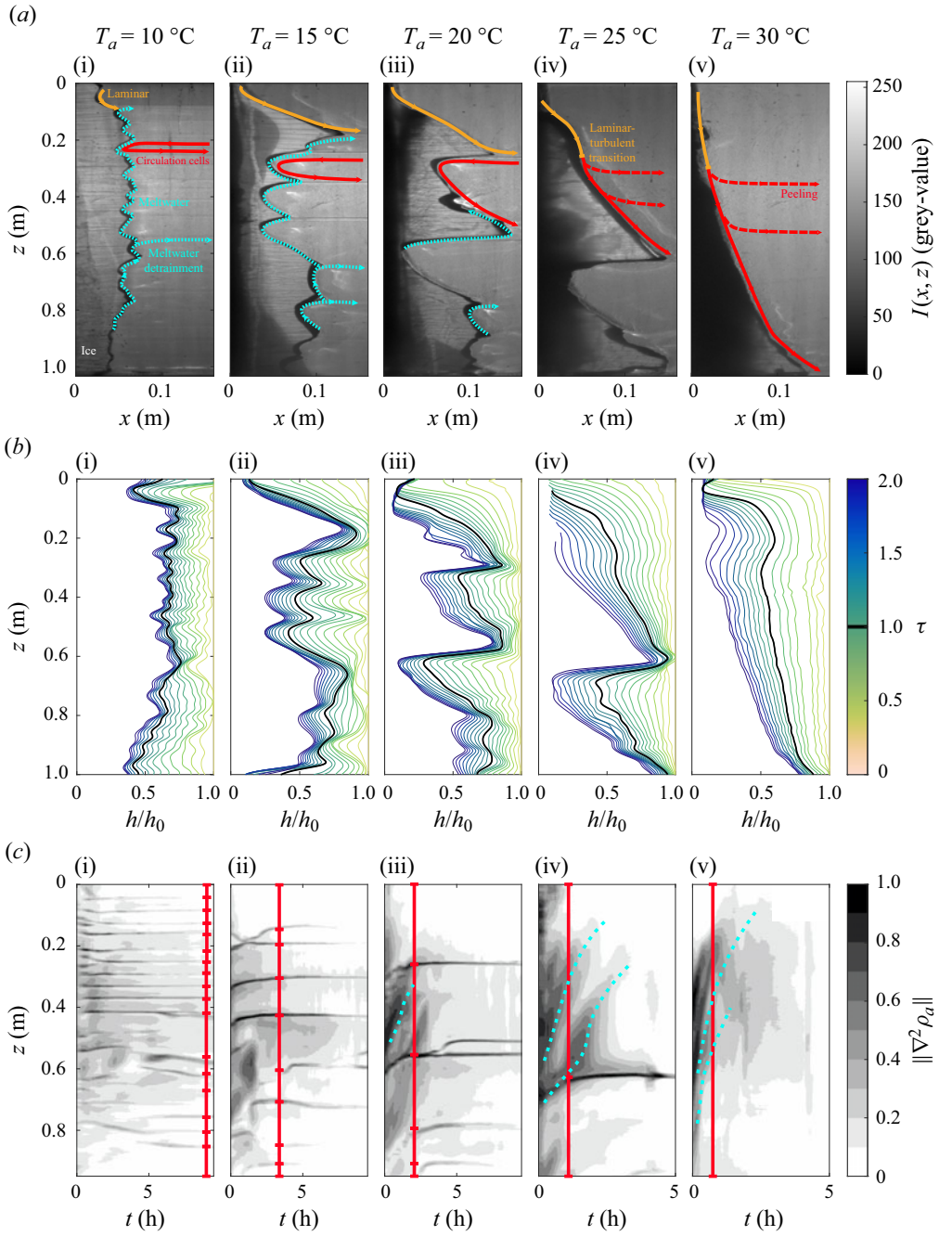

Figure 3. An array of experimental data for experiments with different T_a. (*a*) Characteristic snapshots of the ice (greyscale value $I(x, z)$) at times of proportionally equally melt $t \approx 2\tau$ (refer to table 1), where τ demarcates the time when 1/e of the total fraction of ice has melted. (*b*) Fraction of ice melted in time, where $h(z, t)$ denotes the thickness of ice with respect to its initial thickness h_0. Contours denote one-tenth of a multiple of τ. (*c*) Transient light-field intensity anomalies (proxy for $\nabla^2\rho$) near $x \approx 0.2$ m, useful in the identification of fluid-layer interfaces (solid, markings, $t = \tau$) and plume detrainment (dotted, cyan lines). Columns are ordered by T_a as given in (*a*).

(e.g. Josberger 1979), was observed in our experiments, and as such, we maintain that any sidewall fluxes and boundary effects can be negated from our upcoming analyses.

We find that the formation of ice scallops occurs in conjunction with the development of a 'thermohaline staircase' like fluid layers and associated internal circulation cells. The distinct banded lines in figure 3(*c*) show the strong density interface at the boundaries of these layers, as measured in the observable far field away from the ice face ($\approx$0.2 m). These internal circulation cells (represented by red arrows in figure 3*a*) grow rapidly to the full thickness of each layer and eventually span the length of the tank, as observed over time. We observe a small degree of spatial variability in the depth of the layer interfaces, including merging and splitting events (cf. Radko *et al.* 2014) as well as an initial uplift towards the free surface. The merging and splitting events are a stochastic stabilising mechanism inherent to all thermohaline structures (Radko *et al.* 2014), and the initial uplift behaviour is likely due to the sudden deposition of meltwater into the ambient fluid. In addition to the well-defined density layers, when $T_a > 20\,^{\circ}\mathrm{C}$ additional fluid layers that exhibit a much weaker density interface are also observed. These weak-density interfaces, which shift linearly towards the free surface with time, are identified to be detraining outflows from a 'peeling plume' (cf. Bonnebaigt, Caulfield & Linden 2018). These detraining outflows (see figures 3*a* iv–v) do not appear to affect the melting rate in their local vicinity directly.

Boundary layer flows, both upwelling and downwelling, made evident through the transient light field, were observed in all cases. The relative strength of the boundary layer flow speed was observed to increase with the magnitude of thermal driving. Experiments at lower temperatures ($T_a < 20\,^{\circ}\mathrm{C}$) exhibited a mix of laminar and weakly turbulent downwelling flow in addition to a turbulent upwelling meltwater component, typically between the ice face and the downwelling flow, that was able to penetrate multiple layer interfaces, as illustrated in figures 3(*a* i–ii) (cyan arrows). Experiments with $T_a \geq 20\,^{\circ}\mathrm{C}$ demonstrated a distinctive turbulent boundary layer flow downwelling at the ice–fluid interface, intruding horizontally at either the bottom of the tank or a layer interface (e.g. figure 3*a* iii). For these cases, where multiple layers were present, an immediate transition to turbulence was observed at the ice–fluid interface below the first layer. This behaviour is a result of double-diffusive fluxes across the layer interface, where cold freshwater sits above a warm salty layer, which produces a thermohaline instability (Huppert & Turner 1980; Radko *et al.* 2014). Additionally, the effective thickness of the boundary layer flow ($\delta_m + \delta_a$), which we determined as the point of a sudden decrease in discernible fluid motion in the boundary layer flow away from the ice–fluid interface, was observed to grow with increasing thermal driving. Typical thicknesses were $O(0.5\ \mathrm{cm})$ in the coldest case ($T_a = 10\,^{\circ}\mathrm{C}$), and $O(4\ \mathrm{cm})$ in the warmest case ($T_a = 30\,^{\circ}\mathrm{C}$). We also note that downwelling laminar flows were observed in all cases near the free surface (figure 3*a*, orange arrows), transitioning to turbulence after approximately 10–20 cm alongslope, or at the first layer interface (case-dependent).

3.2. *Layers*

Measurements of the fluid layer thicknesses were made by examining the scallop wavelengths and proxy field for curvature in fluid density, as shown in figures 3(*a*) and 3(*c*), respectively. The stratification length scale is defined as

$$\bar{\eta} = \mathcal{H}\,\Delta\bar{\rho}\left|\frac{\partial \rho_a}{\partial z}\right|^{-1}, \tag{3.1}$$

where $\mathcal{H} = (0.66 \pm 0.06)$ is an empirically determined scaling coefficient, $\Delta\bar{\rho}$ denotes the depth-averaged density difference between the ambient water ρ_a and its respective isohaline freezing point density, and z is the vertical coordinate (HT80). Table 1 summarises the number of layers, their depth-averaged thicknesses compared to the stratification length scale (3.1), and thermal Rayleigh number

$$Ra_Z = \frac{g\alpha\,\Delta T_a\, Z^3}{\nu\kappa_T}, \tag{3.2}$$

where Z is a characteristic vertical length scale, α is the thermal expansion coefficient, ν is the dynamic viscosity, and κ_T is the thermal diffusivity of water, for each of the experiments shown in table 1. We note that all coefficients in (3.2) are evaluated at their respective T_a and $\bar{S}_a$ values. The tabulated results demonstrate that the layer thicknesses are consistent within uncertainty with the theoretical scaling of HT80, albeit with somewhat larger uncertainty at lower ambient temperatures. The empirical scaling coefficient for $\bar{\eta}$ reported by HT80 has known validity in $10^5 \lessapprox Ra_{\bar{\eta}} \lessapprox 10^9$ and for $\bar{\eta} \approx O(50\ \text{mm})$, and is stated to exhibit no systematic dependence on the Rayleigh number beyond the critical value $Ra_{\bar{\eta}} \approx 10^5$ necessary for the development of the layers. To our knowledge, our experiment is the first to investigate vertical ice melting into a salt-stratified fluid with stratification length scales exceeding 0.2 m and $Ra_{\bar{\eta}} > 10^9$, a value slightly beyond the critical transition point to turbulent-free convection (Wells & Worster 2008). From our data, it appears that the empirical scaling coefficient remains valid following the onset of turbulent-free convection up to $Ra_{\bar{\eta}} \approx 10^{11}$. Notably, this value and its global counterpart Ra_H (refer to table 1) are still much less than the critical value 10^{21} for a shear-controlled flux regime (Kerr & McConnochie 2015).

3.3. *Depth-averaged melting rate and steady melting rate assumption*

The depth-integrated melting rate of ice through the entire fluid column is examined using the fraction of ice melted, ϕ, hereafter termed the melt fraction, defined by

$$\phi(t) = 1 - \frac{\displaystyle\int_0^H h(z,t)\,\mathrm{d}z}{A_0}, \tag{3.3}$$

where A_0 is the initial cross-sectional area of ice,

$$A_0 = \int_0^H h_0(z)\,\mathrm{d}z. \tag{3.4}$$

It then follows that the depth-averaged melting rate is defined through

$$\bar{m} = \frac{1}{H}\int_0^H m(z,t)\,\mathrm{d}z = \frac{A_0}{H}\frac{\partial\phi(t)}{\partial t}. \tag{3.5}$$

Figure 4 showcases how the melt fraction is implemented to calculate the depth-averaged melting rate in a state of non-acceleration. We define a characteristic time τ such that $\phi(\tau) = 1/\mathrm{e}$; that is, τ is the e-folding time scale for ice melting (see values in table 1). As shown in figure 4(*a*), the melt fractions for each experiment exhibit similar temporal evolution, with two distinct phases before and after $t \approx \tau$. The first phase is a period of constant melting rate, up to a time τ (which reduces with increasing T_a). The second

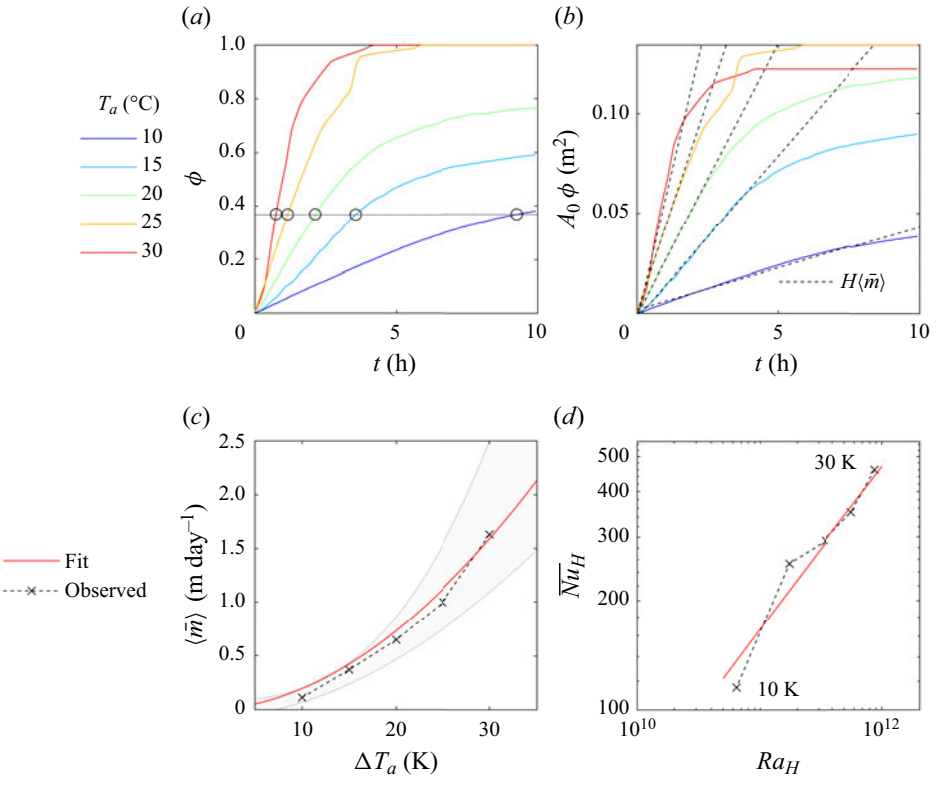

Figure 4. Depth-integrated melting rates: (*a*) net melted-ice fraction $\phi(t)$; (*b*) net melted-ice cross-section with non-accelerating melting rates overlaid (dashed lines); and (*c*) depth-averaged melting rates as a function of thermal driving ΔT_a. Power-law fit (3.7) ($\xi = 2.08 \pm 0.52$) is overlaid. (*d*) Depth-averaged Nusselt number (3.8) as a function of the global Rayleigh number (3.2).

phase involves a gradual reduction in melting rate as the ambient fluid approaches thermal equilibrium and a greater fraction of the heat supplied to the ice must be used for sensible heating rather than melting. We find that this time scale definition is comparable to the inherent time limit τ_0 for an unmaintained ambient fluid temperature field (Malki-Epshtein *et al.* 2004), which indicates that melting for $0 \leq t \leq \tau$ is representative of a constant T_a. We note that the sudden approach of ϕ towards unity for $T_a = 25\,^{\circ}\mathrm{C}$ near $t = 4$ h is due to the calving of the uppermost section of ice from the heat exchanger (cf. figure 3*b* iv). In the following analysis, we focus on the initial non-accelerating melting rate phase.

The depth-integrated melting rate within the linear melting phase is calculated in figure 4(*b*) through a linear fit to (3.5) within the interval $0 \leq t \leq \tau$. Normalising this result by the tank depth H yields the non-accelerating depth-averaged melting rate

$$\langle\bar{m}\rangle \equiv \frac{A_0}{H}\left\langle\frac{\partial\phi}{\partial t}\right\rangle\Bigg|_0^{\tau}, \tag{3.6}$$

where $\langle\cdot\rangle$ denotes a time average (from the linear fit), which is shown in figure 4(*c*) and tabulated in table 1. Here, the depth-averaged melting is shown to have a systematic dependence on the thermal driving consistent with the power-law scaling

$$\langle\bar{m}\rangle = \chi\,\Delta T_a^{\xi}, \tag{3.7}$$

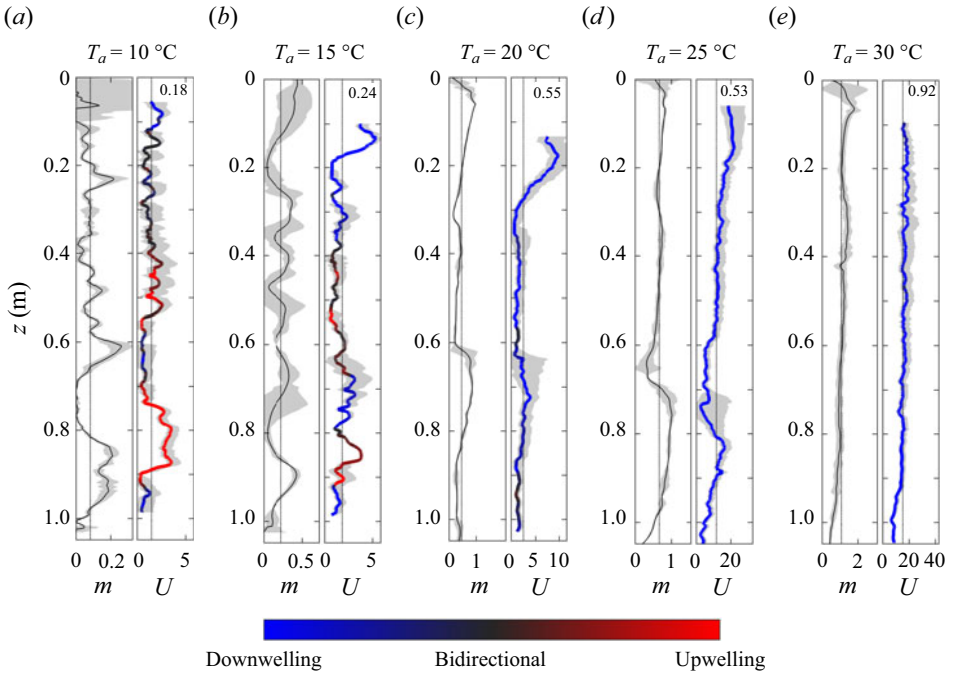

Figure 5. Time-averaged melting rates $m(z)$ (mm min^{-1}), absolute boundary layer flow speed $U(z)$ (mm s^{-1}), and the horizontally averaged flow direction over the effective width of the combined meltwater and ambient fluid boundary layer. The vertical dotted line denotes both $\bar{U}$ and $\bar{m}$. The relative uncertainty in U decreases with increasing T_a owing to the presence of more turbulent small-scale features to track (refer to § 2.3). Correlation coefficients are shown in the upper right corner of each plot.

where χ and ξ are fitting parameters, and $\xi \geq 4/3$ is expected for turbulent flow regimes (Malyarenko *et al.* 2020). Applying (3.7) to the results shown in figure 4(*c*), we find $\chi = 1.29 \times 10^{-3}$ at the centre of the log-log fit, with confidence intervals $\chi = (0.39, 4.77) \times 10^{-3}$ at one standard deviation, and $\xi = 2.08 \pm 0.52$. From these results, we may also estimate the average Nusselt number

$$\overline{Nu}_H = \frac{\bar{h}H}{k_s}, \tag{3.8}$$

where $\bar{h} \approx \langle \bar{m} \rangle \mathcal{L}\rho_s / \Delta T_a$ is the average heat flux, $\rho_s \approx 918$ kg m^{-3} is the density of ice, and $k_s \approx 2.28$ Wm^{-1} K^{-1} is the thermal conductivity of ice. Comparing this to the global Rayleigh number Ra_H (3.2), we observe the power-law scaling

$$\overline{Nu}_H \propto Ra_H^{\mu}, \tag{3.9}$$

where $\mu = 0.45 \pm 0.19$, as shown in figure 4(*d*). We will compare these scalings with those from previous work in the discussion ahead, and hereafter drop the time-averaging notation for clarity.

3.4. *Depth-dependent melting rates and boundary layer flow speeds*

The melting rates and the absolute maximum boundary layer flow speed as a function of depth, averaged over times $0 \leq t \leq 1$ hr, are shown in figure 5, where calculation of the

depth-dependent melting rates was extracted from the time-derivative field of figure 3(*b*). Our first general observation is that contrary to expected melting rate behaviour (cf. Magorrian & Wells 2016), no significant imprint on the peak melting rates can be inferred from the far-field salinity profile. We speculate that this large-scale depth-dependent melting rate behaviour is not pronounced in our experiments due to the relatively weak imposed salinity gradient and high thermal driving limit, wherein any depth-wise variation in the salt fluxes to the ice–fluid interface through the fluid column is masked by the substantially larger heat fluxes. Second, we find the behaviour of the boundary layer flow to be broadly consistent with the expected dynamics summarised by Carey & Gebhart (1982), mentioned in § 2.4, also considering the inclusion of a salinity gradient. As shown in figure 5, bidirectional flows are prevalent throughout the fluid column at lower thermal driving temperatures, which steadily become downwelling unidirectional flows as the thermal driving increases.

Upwelling meltwater plumes, as shown in figures 5(*a*) and 5(*b*) (red shadings on the flow speed profile), are readily identifiable only in the colder cases ($T_a \leq 15\,^{\circ}\mathrm{C}$). In the coldest case (figure 5*a*), the coherent patches of upwelling correspond to a mostly turbulent plume, but as these upwell, they thin progressively into a laminar plume (between upwelling and bidirectional flow) through detrainment with the ambient fluid plume and penetration across multiple layer interfaces, consistent with the dynamics reported by HT80. When the meltwater plume has thinned back to a laminar plume, we observe a bidirectional flow with the ambient fluid that is of comparable flow speed in either opposite direction. By contrast, as the ambient temperature is increased ($T_a \geq 20\,^{\circ}\mathrm{C}$), we find that bidirectional and upwelling flows are practically non-existent, and downwelling prevails next to the ice face over the full depth. Mean flow speeds are observed to increase with thermal driving, consistent with the expectations of naturally convecting systems, with the warmest case (20 mm s^{-1}) an order of magnitude faster than the coldest case (1.5 mm s^{-1}; see table 1). We observe that flow speeds tend to reduce slightly but systematically over the course of the experiment, but this reduction remains within the margin or error shown in figure 5. In the warmer cases where downwelling flow is dominant and turbulent free convection is established ($T_a \geq 20\,^{\circ}\mathrm{C}$), our results show that the local melting rate generally mirrors the observed flow speed profile; that is, $m \propto U$, from inspection and also interrogation via the correlation coefficients (as shown in figure 5), having accounted for the uncertainty bounds. This relationship appears to be more consistent with the flow dependence found in a shear-controlled regime rather than a buoyancy-controlled scaling where $m \propto U^{2/3}$ can be derived (Kerr & McConnochie 2015; Malyarenko *et al.* 2020). In the transitional laminar flow regime near the surface ($z < 0.3$ m), where flow speeds are substantially larger than the deeper turbulent flow, the melting rates also appear to mirror the flow speeds, albeit with a different scaling; for instance, figures 5(*b*) and 5(*c*) show a pronounced enhancement in the flow speed near the surface while the melting rate is broadly consistent with that of the deeper ice. These observations are consistent with the notion that turbulent fluxes melt ice more efficiently than laminar fluxes via greater shear stresses, even though the flow speed in the laminar flux regime can be faster (Hewitt 2020; Hester *et al.* 2021). However, at lower thermal driving ($T \leq 15\,^{\circ}\mathrm{C}$), our data exhibit no clear relationship between flow speed and melting rates, possibly in part owing to the large uncertainty in flow speed measurements at these temperatures. Furthermore, in figure 5(*b*) there is a near zero melting rate ($m < 5 \times 10^{-2}$ mm min^{-1}) at $z \approx 0.7$ m despite a significant flow speed ($U \approx 3$ mm s^{-1}). The likely explanation is that ambient heat fluxes to the ice are being strongly suppressed due to the build up of meltwater in that

fluid layer, as this region is observed to be dominated by upwelling and laterally intruding meltwater (see figure 3*a* i).

4. Discussion

We have presented novel results for melting a vertical ice face in a warm, salt-stratified environment. We now consider how our depth-averaged results compare to those reported for other parameter regimes, primarily as functions of thermal driving but also in terms of the buoyancy frequency, and explore the power-law fit exponents. Following this, we consider the depth-dependent melting via turbulent flux regime scalings and possible explanations for the observed scalloping behaviour. Finally, we discuss the implications of our results and possible avenues for future work.

4.1. *Depth-averaged melting*

As demonstrated, our salt-stratified experiments indicate that the thermal driving dependent power-law parametrisation is still a valid representation of depth-averaged melting rates in stratified environments. However, owing to the many practical challenges involved with laboratory experiments, there are limited data on stratified melting rates as functions of thermal driving to benchmark our results, but sufficient data regarding melting into unstratified environments. The only suitable reference for stratified melting is also the most commonly used scaling for sidewall melting due to natural buoyant convection, based on a revised melting rate scaling determined from observations and statistics of icebergs located in d'Iberville Fjord, as studied originally by Morgan & Budd (1978) and revised by Neshyba & Josberger (1980) (NJ80). However, except for the novel phase-changing simulations (PCS) experiments from Wilson *et al.* (2023) (W23), additional stratified melting rate data exist only through a salinity gradient parameter space, albeit these are sparsely represented in the thermal driving space: notably, the laboratory results from McConnochie & Kerr (2016) (MK16) and HT80, and recent PCS experiments from Yang *et al.* (2023) (Y23). By contrast, unstratified melting rates have been reported from Josberger & Martin (1981) (JM81), Johnson & Mollendorf (1984) (JM84), Dutton & Sharan (1988) (DS88) and Kerr & McConnochie (2015) (KM15). The NJ80 observation-based scaling predicts lower melting rates at higher ambient temperatures compared with successive laboratory work (i.e. JM81, JM84, DS88; see figure 6). We note that for JM84 and DS88, no scalings were reported, but we have determined them from the graphed melting rate and Nusselt number data, conducted at differing reference salt concentrations (labelled as * in table 2). Similarly, the HT80 singular data point was determined as the average one-sided, depth-averaged melting rates from the single experiment available in photographic form as a time series from their study, using techniques similar to those described in § 2.

Regarding only the real-world data, our salt-stratified experiments are consistent with the NJ80 scaling and HT80 experiment, and through extrapolation, overlap with the MK16 data. Despite the differences in scale and driving conditions (refer to table 2), this outcome points to the crucial importance of stratification in setting iceberg melting rates. Previously, to account for the disparity between the JM81 laboratory experiment scalings and NJ80 revised observational scalings, it was proposed that a depth-dependent term $H^{-1/4}$ (where H represents the keel depth measured from the transition point of turbulent-free convection for an unstratified fluid) was needed to extrapolate the scaling into more geophysically relevant length scales and Grashof numbers. This term, derived

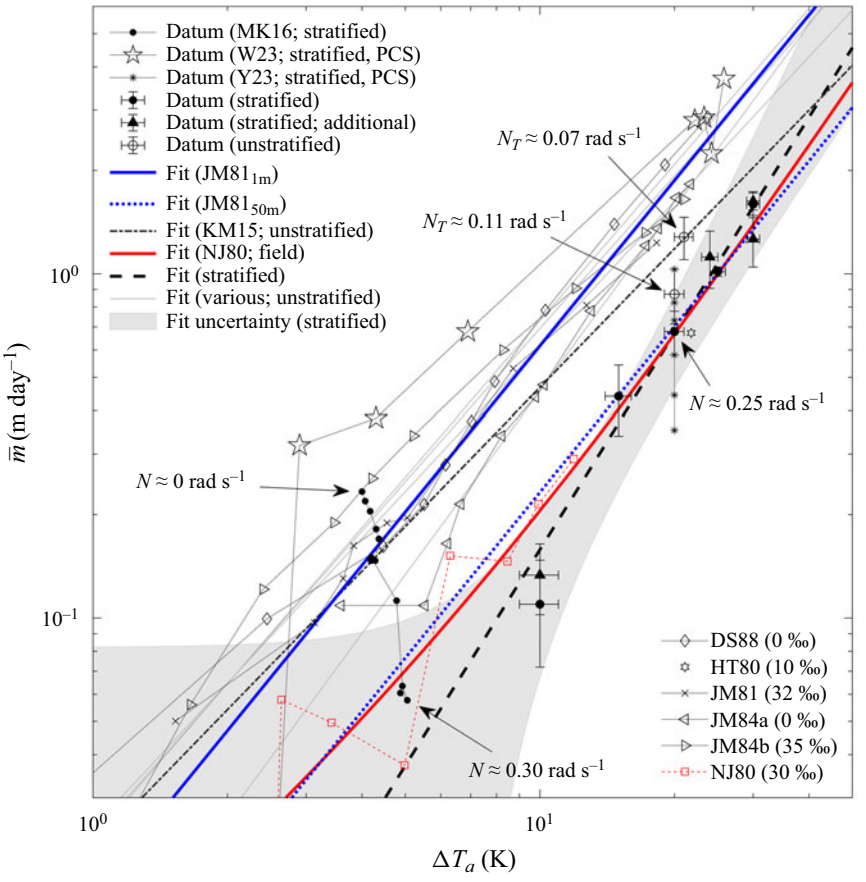

Figure 6. Depth-averaged melting rate data and power-law fits from current and previous work as listed in table 2. Labelled thermal buoyancy frequencies N_T are calculated at $t \approx \tau$. Note the melting rate data as a function of N from MK16 (endpoints labelled), whereas Y23 data are grouped averages for a constant salinity gradient ($\bar{m}$ decreases with increasing $\partial S_a/\partial z$).

Authors	$\chi \times 10^{-3}$	ξ	Source	H (m)	ΔT_a (K)	$\overline{S_a}$ (‰)
Present study	1.3	2.1	Lab	1.1	10–30	0–10
Neshyba & Josberger (1980) (NJ80)	5.9	1.54	Obs	$O(200)$	0–10	28–32
Josberger & Martin (1981) (JM81$_{1m}$)	24.5	1.40	Lab	1.25	0–27	29–35
Josberger & Martin (1981) (JM81$_{50m}$)	$H^{-1/4}15.5$	1.60	Lab	1.25	0–27	29–35
Johnson & Mollendorf (1984) (JM84a*)	7.7	1.77	Lab	0.3	1–21	0
Johnson & Mollendorf (1984) (JM84b*)	22.6	1.51	Lab	0.3	1–21	35
Dutton & Sharan (1988) (DS88*)	23.1	1.47	Lab	0.7	1–9	0
Kerr & McConnochie (2015) (KM15)	21.4	1.34	Lab	0.7	0–6	2–37
Wilson *et al.* (2023) (W23)	5.47	2.07	PCS	0.15–1.2	0.4–26	8–35
Huppert & Turner (1980) (HT80*)	—	—	Lab	0.25	21.8	10
McConnochie & Kerr (2016) (MK16*)	—	—	Lab	1.1	4–6	34–37
Yang *et al.* (2023) (Y23*)	—	—	PCS	0.1	20	0–15

Table 2. Various reported and calculated/collected (*) depth-averaged melting rate power-law scalings and data (in metres per day), as showcased in figure 6. The uncertainties for this study, $\chi = (0.39, 4.8)$, $\xi = \pm 0.52$, are at one standard deviation.

from a 'laminarised' turbulent similarity theory coupled with laboratory observations (where $m(z) = 1.55 \times 10^{-2}\,\Delta T_a^{8/5}\,z^{-1/4}$) and averaging over the keel depth, shows improved agreement with the melting rate scaling reported by NJ80, as demonstrated when $H \approx 50$ m in figure 6. Additional reported scalings from unstratified laboratory experiments seem to be consistent with the JM81 melting rates, including the freshwater and typical seawater salt concentration results from JM84, freshwater depth-integrated Nusselt number results of DS88, and also the extrapolated dissolving regime ($T_a \lessapprox 6\,^\circ$C) results from KM15 (albeit up to $\Delta T_a \approx 10$ K). However, the JM81 unstratified scaling argument conflicts directly with geophysical environments, which are stratified. Though the stratification in most polar oceans is exceptionally weak ($N \approx O(1 \times 10^{-3}$ rad s^{-1})), the vertical length scales of icebergs or glaciers are conversely large ($H \approx O(1 \times 10^2$ m); HT80). This consideration poses the question of how relatively stratified an environment must be before melting rates depart significantly from the unstratified scalings.

For geophysically relevant conditions, MK16 argued that, at least for salt-stratified environments, there exists a threshold buoyancy frequency N_c that demarcates the unstratified scaling. Their results (see figure 6) demonstrated that the rate at which the depth-averaged melting rate decreases with N is nonlinear, maximised in unstratified conditions, and minimised at larger N (at least up to 0.3 rad s^{-1}). Using a scaling analysis based on plume theory's description of the meltwater plume buoyancy flux decreasing with height due to stratification, an expression to determine N_c for any vertical length scale was derived. In a laboratory-sized domain ($O(1$ m)) for low thermal driving conditions, melting rates based on unstratified theory would become increasingly inaccurate if a critical buoyancy frequency N_c were to exceed 0.04 rad s^{-1}. However, there is reason to debate whether the MK16 argument is translatable directly to a parameter space where the ambient fluid component of the boundary layer also contributes meaningfully to the alongslope flow and melting dynamics. Recently, the novel PCS experiments of Y23 demonstrated that the relationship between depth-averaged melting and the salinity gradient and mean salinity is non-monotonic. When averaged by mean salinity (shown in figure 6), their results show that increasing the salt stratification tends to suppress the depth-averaged melting rates relative to an unstratified case almost linearly; no critical buoyancy frequency threshold was apparent.

Our results loosely support this overall dependence on the buoyancy frequency. We note, per tables 1 and 3, that all of our salt-stratification experiments had an initial stratification where N was greater than N_c. To confirm the crucial importance of stratification, we also conducted two additional experiments with non-salt-stratified fluids. In these additional experiments, conducted at $T_a \approx 20\,^\circ$C, one was left to develop a thermal stratification, $N_T^2 \propto \partial T_a/\partial z$, whereas the other was replenished continuously with ambient fluid to maintain a homogeneous temperature field (however, a weak thermal stratification was observed). These two reference cases demonstrate that a salt or thermal stratification impacts the depth-averaged melting rates (as labelled in figure 6), with increasing stratification acting to decrease the melting rate. According to our limited data, we find no significant difference between a thermally stratified and salt-stratified melting regime at high thermal driving, and concur that actively maintaining a homogeneous fluid yields melting rates that are more consistent with other homogeneous parametrisations. Our results indicate that at conditions of high thermal driving, the role of a salt stratification appears to both partition the thermal fluxes into discretised layers and suppress the depth-averaged melting rate through the resultant interior thermal stratification (cf. Worster & Leitch 1985; Cooper & Hunt 2010; Wilson *et al.* 2023). Regarding the recent

novel PCS experiments (Y23 and W23) that emulate a laboratory set-up and include a salt-stratified environment, the W23 reported findings appear to be broadly consistent with the melting rates of all other unstratified laboratory experiments at conditions of high thermal driving, whereas the Y23 results show general agreement with our results. The likely explanation for the disparity between the W23 results and our data stems from their model configuration, which required unrealistically strong heat and salt diffusivities to be adopted (by a factor of 3 in terms of the heat-to-salt diffusivity ratio). By contrast, Y23 used a more realistic set of diffusive parameters.

Regarding the fitting coefficients from the power-law scaling (3.7), the values presented in table 2 show general agreement that $4/3 \leq \xi \leq 2$ are appropriate bounds for the exponent, barring some uncertainty. To explore why these bounds exist, we may consider the scalings posed through the turbulent-flux regimes (Malyarenko *et al.* 2020), which indicate that the depth-averaged melting rate can be expressed through

$$\bar{m} \propto \Delta T_a \begin{cases} \bar{b}^{1/3}, & \text{buoyancy-controlled,} \\ \bar{U}, & \text{shear-controlled.} \end{cases} \tag{4.1}$$

For simplicity, by assuming that the average buoyancy in a salt-stratified environment is mostly constant throughout the entire fluid column, and the dominant force balance is between thermal buoyancy ($g\alpha\Delta T_a$) and inertia (U^2/Z, where Z is a characteristic vertical length scale Malki-Epshtein *et al.* 2004), such that

$$\bar{b} = g\alpha\, \Delta T_a \propto \frac{\bar{U}^2}{\bar{\eta}}, \tag{4.2}$$

where $\bar{\eta} \propto \Delta T_a\, (\partial\rho_a/\partial z)^{-1}$ from (3.1), it also follows that the scalings in (4.1) are of the form

$$\bar{m} \propto f(\bar{U})\, \Delta T_a, \tag{4.3}$$

where $f(\bar{U})$ is a function of the flow speed, which is consistent with other melting rate parametrisations (Hewitt 2020). For the buoyancy-controlled regime, (4.2) implies that $f(\bar{U}) \propto (\bar{U}^2/\Delta T_a)^{1/3}$. Furthermore, assuming that the flow is driven primarily by thermal processes for both turbulent-flux regimes from the ambient fluid (i.e. $\bar{U} \propto \Delta T_a$), flow-independent scalings can be deduced using (4.1), where $\xi = 4/3$ for buoyancy-controlled regimes, and $\xi = 2$ for shear-controlled regimes. From these assumptions, ξ is implied to represent a product of linear thermal driving and a nonlinear velocity term that scales with ΔT_a. As we determined $\xi = 2.1 \pm 0.52$ (see table 2), this would imply that the exponent for the flow speed component, $f(\bar{U})^{\xi-1}$, is approximately 1.1 ± 0.52. This value conflicts with our expected buoyancy-controlled flow speed relation exponent $1/3$, but has better agreement with the exponent value $4/5$ found in forced convection (Weeks & Campbell 1973) and a thermally driven, shear-controlled regime value. Moreover, we remark that the exponent found in the average Nusselt number, $\mu = 0.45 \pm 0.19$, is also more consistent with that of a shear-controlled regime ($\mu = 1/2$) than a buoyancy-controlled regime ($\mu = 1/3$; Malyarenko *et al.* 2020). However, we caution that fitting a power law to data that do not include melting rates below 10 °C and have minor variability in N is insufficient to ascertain an accurate ξ value, and warrants further investigation using a broader parameter space. In particular, ξ and χ are unlikely to be constant, and furthermore, both could depend on N (as may be inferred from MK16 and Y23), $\bar{S}_a$ (following inspection of the JM84 and KM15 scalings, and that reported within Y23) and H (JM81).

4.2. *Depth-dependent melting*

Our results demonstrated a positive correlation between the flow speed and local melting rate throughout the fluid column, most prominently at conditions of higher thermal driving where the flow exhibited turbulent-free convection. As noted previously, this behaviour is more consistent with a shear-controlled flux regime than the buoyancy-controlled regime that we anticipated (Malyarenko *et al.* 2020). In our experiments, the boundary layer flow did not exceed the threshold 30 mm s^{-1} or the critical Rayleigh number 10^{21} that is suggested to delineate a transition from buoyancy-controlled to shear-controlled regimes (Kerr & McConnochie 2015). A possible reason for the anomalous scaling is that the definition of a buoyancy-controlled flux regime is not strictly valid for the ambient fluid component of the boundary layer flow, at least in a stratified environment where double-diffusive circulation is present. For example, potentially an established circulating flow could promote a self-sustaining forced convection scheme where the turbulent fluxes of the ambient flow component fall into a shear-controlled regime, leading to a $\xi = 2$ exponent if the circulation is derived from thermal processes (4.1). However, more definitive measurements of the flow field and acquisition of streamfunctions would be required to support this hypothesis. We note that our measurements could not resolve reliably the flow dependence along the ice–fluid interface at all depths, especially at lower thermal driving temperatures in laminar-free convection cases, through shadowgraph techniques alone. Despite the practical accessibility of the shadowgraph method, the inclusion of particle image velocimetry techniques would certainly improve the fidelity of the flow field and boundary flow measurements.

As for the resultant ice scalloping patterns, while we do not have a complete physical explanation for the observed flow speeds and resulting melting rates, we can speculate about the processes driving their formation. It is clear that the scallops are strongly related to the impinging ambient fluid flow from the flow speed measurements (figure 5). As demonstrated from the experiments of MK16 and W23, the imprint of the scallops tends to become suppressed when $\Delta T_a < 6$ K, due primarily to the boundary layer flow dynamics being dominated by the meltwater plume. Similarly, Y23 also showed that as $N \gtrapprox 1$ rad s^{-1}, where the stratification length scale becomes relatively small compared to the height of the system (i.e. $\bar{\eta}/H \ll 1$), there is a reduction in the scallop amplitudes owing to an overall weakening of the boundary layer flow speed. However, it may also be argued that increasing the stratification length scale through a reduction in the salinity gradient, which causes the average ambient fluid plume velocity to increase (see (4.2)), would increase the melting rate through increased turbulent shear stresses. Given that the different scalloping patterns (figure 3*a*) seemingly do not affect the depth-averaged melting rates in terms of departing from the power-law parametrisation (figure 6), we speculate that the process for setting the predominant scalloping shape is related to the momentum flux of the flow impinging on the ice–fluid interface, which could modify how the heat flux budget within a layer is distributed as it travels downslope (e.g. Magorrian & Wells 2016). Detailed knowledge of the boundary layer flow speed and its temperature and salinity would be required to constrain this behaviour further.

4.3. *Scaling, application, and remarks*

The application of our laboratory results to the ocean requires careful consideration. The fact that our depth-averaged melting rates generally agreed with the NJ80 field observation parametrisation raises the question of what factors contributed to this result.

As mentioned previously, our parameter space occupies a different dynamical regime wherein the meltwater and ambient fluid plumes contribute to the boundary layer flow (temperature–salinity dependent), and the stratification length scale is also a relevant factor. In the laboratory, the inevitably smaller vertical length scales mean that we are always dealing with significantly larger stratifications than in the ocean to achieve a sufficient buoyancy difference to capture the double-diffusive dynamics of interest. If we assume that the total buoyancy difference in the laboratory is equivalent to that across an iceberg in the ocean (i.e. $N^2_{lab}H_{lab} = N^2_{ocean}H_{ocean}$), then we can estimate that the difference in scales is comparable (cf. HT80). However, it is still unclear how the large difference in mean salinity and global Rayleigh numbers could yield similar melting rates.

In terms of applicability, our results suggest that future modelling and observational studies on drifting icebergs or glaciers should take note of the potential influence of stratification on the depth-averaged melting rate. In sufficiently low stratification environments, melting rates could likely depart from the commonly used NJ80 scaling, meaning that calculations could potentially significantly underestimate total melting. This departure could be more relevant for freshwater harvesting operations, where icebergs could be towed into warmer and possibly fresher waters. Moreover, our results also highlight the need for improved high-resolution models (e.g. Wilson *et al.* 2023; Yang *et al.* 2023), as there appears to be clear sensitivity in the thermal and salt diffusivity parameters on the melting rates.

Finally, we remark on the future work needed to deepen our understanding of the continuum between melting into stratified and unstratified environments. It is clear from our experiments that the flow regimes posed by Carey & Gebhart (1982) provide a useful guide for predicting the expected flow dynamics in a salt stratification, requiring some adjustments to explain precisely where unidirectional and bidirectional flows may coexist throughout the fluid column due to a salinity gradient. Greater investigation into the salt-stratification space at different reference salinities would help to uncover the dependence on the buoyancy frequency for the coefficients in the power-law parametrisation, possible variation to the threshold buoyancy frequency in salinity space, and interplay between flow regimes and the scalloping. Finally, there is a clear gap needing to be filled in plume theory to accommodate double-diffusive convection and the bidirectional meltwater and ambient fluid plumes to explain the interplay between melting and flow dynamics fully.

5. Conclusions

In this study, we performed experiments to assess vertical ice's melting rates and morphological response in a warm salt-stratified fluid of low salt concentration. In these experiments, a weak salinity gradient and variable ambient far-field temperatures ranging from 10 °C to 30 °C were imposed, enforcing a melting regime where buoyancy in the ambient fluid component of the boundary layer is chiefly thermally controlled. We observed characteristic melting patterns repeating across the ice face, commonly referred to as scallops, at wavelengths in proportion to the ambient fluid stratification length scale $\bar{\eta}$ defined by Huppert & Turner (1980). As the thermal driving was increased, $\bar{\eta}$ also increased, and the scalloping exhibited a change between experiments from a symmetric profile to an asymmetric sawtooth profile. The boundary layer, composed of meltwater and ambient fluid components, exhibited a mix of unidirectional and bidirectional flow regimes, in general agreement with the expectations given by Carey & Gebhart (1982). Measurements of the boundary layer flow speed showed that the asymmetric melting

was associated with a similarly shaped flow speed profile, i.e. $m \propto U$. We hypothesise that this asymmetric flow evolves due to a combination of turbulent entrainment of the boundary layer flow scaling with the heat flux from the ambient fluid, and interaction with the thermal stratification interior to a layer. Our local melting rates were consistent with the Jenkins (2011) parametrisation that $m \propto U$, and in a depth-averaged sense, the power-law parametrisation $\bar{m} = \chi\, \Delta T_a^{\xi}$, where $\chi \approx 2 \times 10^{-3}$ m day^{-1} K$^{-\xi}$ and $4/3 \leq \xi \leq 2$, in agreement with Neshyba & Josberger (1980). We have demonstrated that stratification is important in setting the depth-averaged melting rate, which may be considered broadly consistent with the arguments posed by McConnochie & Kerr (2016) that unstratified power-law scalings become inaccurate beyond a critical buoyancy frequency. Our results thus extend the demonstrated range of validity of the stratified power-law parametrisation to weakly salt-stratified environments of low salt concentration. Moreover, our results have implications for numerical studies that intend to reproduce laboratory-scale melting rates, in particular, the importance of setting appropriate diffusive parameters, and the representation of iceberg morphology in warm double-diffusive environments for freshwater harvesting operations, where turbulent-free convection has a systematic effect on the local melting behaviour. However, future work is necessary to fully understand the influence of salt stratification on vertical ice melting rates.

Funding. The authors would like to acknowledge the technical support provided by Mr A. Rummery in designing and constructing the modified double-bucket system, and Mr P. Lanc for developing the mixing valve control software.

Declaration of interests. The authors report no conflict of interest.

Author ORCIDs.
James K. Sweetman https://orcid.org/0009-0005-7963-0957;
Callum J. Shakespeare https://orcid.org/0000-0002-8109-0751;
Kial D. Stewart https://orcid.org/0000-0002-9947-1958;
Craig D. McConnochie https://orcid.org/0000-0001-7105-192X.

Appendix A

A.1. *Additional observations*

In addition to the parameter space sampled in the main text, five more experiments were conducted at different salt concentrations, listed in table 3, including two reference experiments without a salt stratification ($\bar{S}_a = 0$ ‰).

A.2. *Methodology for unstratified experiments*

As described in the main text, the technique for maintaining a homogeneous ambient temperature requires the fluid to be replenished during experimentation constantly, otherwise densified ambient water accumulates at the bottom of the tank, akin to a filling box model, and creates a thermally stratified fluid, $N_T^2 = g\alpha\, \partial T_a/\partial z$. In this situation, we would expect that the depth-averaged melting rate is then suppressed by the thermal stratification, in the same manner as by salt stratification. To test this stratification effect, we adapted the experimental design detailed by Josberger & Martin (1981). Our set-up (as shown in figure 7) differs from that of Josberger & Martin (1981) in not requiring an external heating reservoir (at the expense of considerable water usage). We partition a region of the tank to become a large reservoir, partially sealed by a thick highly porous medium (diffusing screen), and replenish the reservoir with tap water at the

T_a (°C)	30	30	24	10	20	20
S_0 (‰)	5	5	0	0	0	0
$\bar{S}_a$ (‰)	7.5	10	1	5	0	0
$\partial S_a/\partial z$ (‰ m^{-1})	5.5	11	2.2	5.5	0	0
N (rad s^{-1})	0.18	0.26	0.11	0.26	0.11	0.07
$\langle \bar{m} \rangle$ (m day^{-1})	1.63	1.23	1.11	0.13	0.87	1.28

Table 3. List of supplementary experimental parameters and depth-integrated melting rates. Buoyancy frequencies are referenced with respect to the dominant stratifying species (haline or thermal).

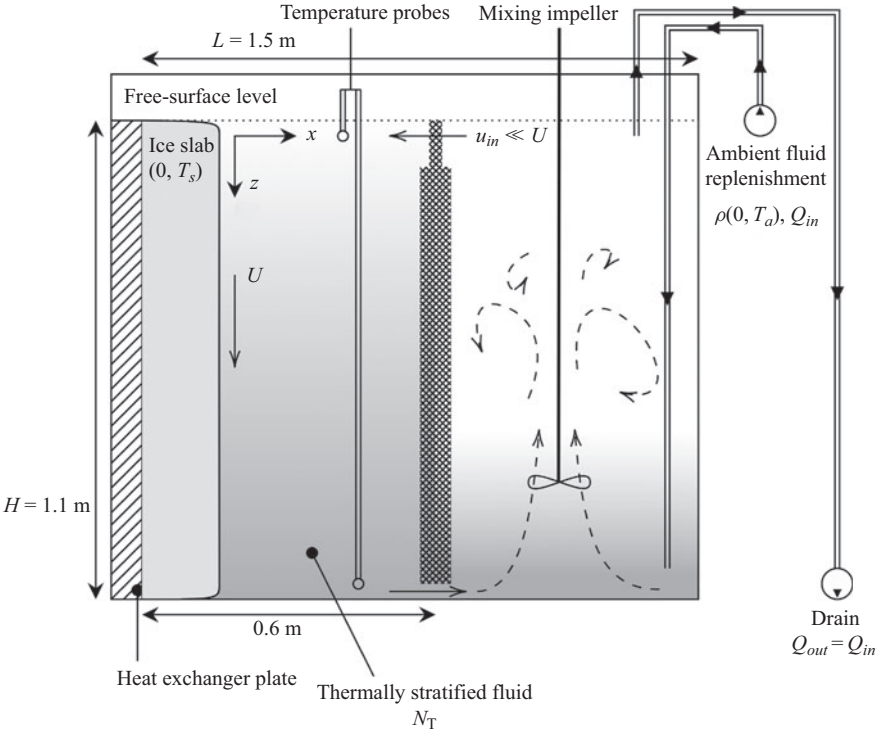

Figure 7. Schematic of the experimental set-up for an unstratified experiment.

prescribed ambient temperature T_a at flow rate $Q_{in} \approx 13$ l min^{-1}. Simultaneously, the reservoir would be drained at an equal rate Q_{out}. At the bottom of the tank was a small opening to allow densified ambient water into the reservoir at a moderate flow rate $\approx$2 l min^{-1} and mixed by an impeller. A thinner diffusing screen at the top of the tank allowed an approximately equal flow out of the reservoir into the experiment chamber. Two temperature probes were placed at the top and bottom of the tank, approximately 0.1 m from the diffusing screen, sampling every 5 min. Despite this attempt to maintain a homogeneous ambient fluid, a weak thermal stratification -3 K m^{-1} developed steadily during experimentation, corresponding to $N_T \approx 0.07$ rad s^{-1}. For comparison, we also tested a case without the Josberger & Martin (1981) set-up where the densified ambient fluid naturally developed a (significantly larger) thermal stratification 0.11 rad s^{-1}. These experiments' depth-averaged melting rate results are reported in § 3 and discussed in

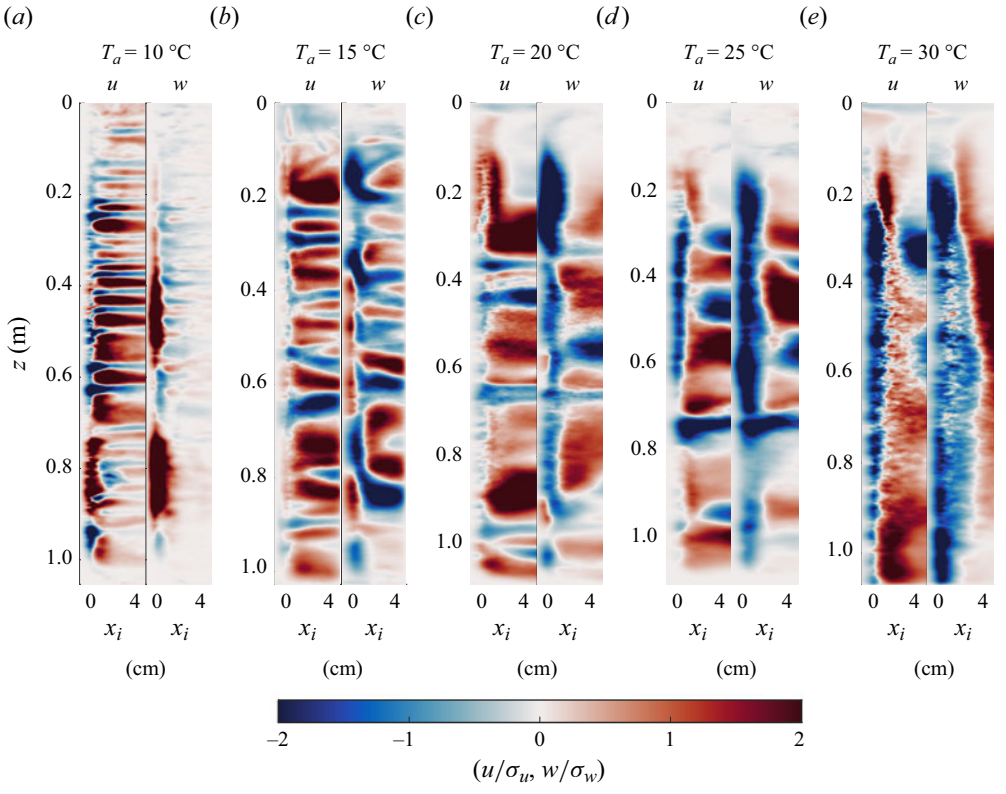

Figure 8. Time-averaged velocity fields (across $0 \leq t \leq 1$ h) extracted from the Optical Flow software package in an ice-normal coordinate system (x_i denotes the distance from the interface in centimetres). Horizontal and vertical components (u, w) are normalised with respect to the standard deviation of the respective field σ.

§ 4. Despite our inability to produce a fully unstratified experimental configuration, these results provide sufficient evidence to interpret the differences between the melting rates in our primary salt-stratified experiments and previous results in unstratified environments.

A.3. *Fluid velocity: optical flow*

Additional fluid velocity measurements were taken through the software package Optical Flow (Liu & Salazar 2021) to characterise the entire flow field. To ensure that the representation of the flow field was not spatially invariant due to the melting of the ice face, we adopted a pseudo-ice-normal coordinate system by shifting the global horizontal coordinate to the ice face, such that $x_i(z, t) = x - h(z, t)$. The time-averaged ($0 \leq t < 1$ h) and normalised horizontal and vertical velocity components are shown in figure 8. As mentioned in § 2.3, usage of this analysis technique was limited to qualitative insights for the flow field, and assisted in the acquisition of the average boundary layer flow direction (the effective plume width is approximately contained in $0 \leq x_i \lessapprox 4$ cm). This decision was made chiefly due to quantitative inconsistencies in the representation of the boundary layer, which, while directionally correct, could not be appreciably tuned to reliably correlate high-speed regions of the plume that demonstrated vigorous turbulence. An example of this can be seen in figure 8(*d*) near $z = 0.75$ m in the vertical velocity field, where the downwelling ambient fluid rapidly decreases further downslope (cf. figure 5*d*).

References

ALLEY, R.B., CLARK, P.U., HUYBRECHTS, P. & JOUGHIN, I. 2005 Ice-sheet and sea-level changes. *Science* **310** (5747), 456–460.

BAINES, P.G. 2002 Two-dimensional plumes in stratified environments. *J. Fluid Mech.* **471**, 315–337.

BIGG, G.R., WADLEY, M.R., STEVENS, D.P. & JOHNSON, J.A. 1997 Modelling the dynamics and thermodynamics of icebergs. *Cold Reg. Sci. Technol.* **26** (2), 113–135.

BONNEBAIGT, R., CAULFIELD, C.P. & LINDEN, P.F. 2018 Detrainment of plumes from vertically distributed sources. *Environ. Fluid Mech.* **18**, 3–25.

BUSHUK, M., HOLLAND, D.M., STANTON, T.P., STERN, A. & GRAY, C. 2019 Ice scallops: a laboratory investigation of the ice–water interface. *J. Fluid Mech.* **873**, 942–976.

CAREY, V.P. & GEBHART, B. 1982 Transport near a vertical ice surface melting in saline water: experiments at low salinities. *J. Fluid Mech.* **117**, 403–423.

CENEDESE, C. & STRANEO, F. 2023 Icebergs melting. *Annu. Rev. Fluid Mech.* **55**, 377–402.

COOPER, P. & HUNT, G.R. 2010 The ventilated filling box containing a vertically distributed source of buoyancy. *J. Fluid Mech.* **646**, 39–58.

DOWDESWELL, J.A. & BAMBER, J.L. 2007 Keel depths of modern Antarctic icebergs and implications for sea-floor scouring in the geological record. *Mar. Geol.* **243** (1–4), 120–131.

DUTTON, C.R. & SHARAN, A.M. 1988 A study of the heat transfer process in fresh water at low temperatures. *Cold Reg. Sci. Technol.* **15** (1), 13–22.

HESTER, E.W., MCCONNOCHIE, C.D., CENEDESE, C., COUSTON, L.-A. & VASIL, G. 2021 Aspect ratio affects iceberg melting. *Phys. Rev. Fluids* **6** (2), 023802.

HEWITT, I.J. 2020 Subglacial plumes. *Annu. Rev. Fluid Mech.* **52**, 145–169.

HUPPERT, H.E. & TURNER, J.S. 1980 Ice blocks melting into a salinity gradient. *J. Fluid Mech.* **100** (2), 367–384.

JENKINS, A. 2011 Convection-driven melting near the grounding lines of ice shelves and tidewater glaciers. *J. Phys. Oceanogr.* **41** (12), 2279–2294.

JOHNSON, R.S. & MOLLENDORF, J.C. 1984 Transport from a vertical ice surface melting in saline water. *Intl J. Heat Mass Transfer* **27** (10), 1928–1932.

JOSBERGER, E.G. 1979 Laminar and turbulent boundary layers adjacent to melting vertical ice walls in salt water. *Tech. Rep.* Washington University, Seattle, Department of Atmospheric Sciences.

JOSBERGER, E.G. & MARTIN, S. 1981 A laboratory and theoretical study of the boundary layer adjacent to a vertical melting ice wall in salt water. *J. Fluid Mech.* **111**, 439–473.

KARIMIDASTENAEI, Z., KLÖVE, B., SADEGH, M. & HAGHIGHI, A.T. 2021 Polar ice as an unconventional water resource: opportunities and challenges. *Water* **13** (22), 3220.

KERR, R.C. & MCCONNOCHIE, C.D. 2015 Dissolution of a vertical solid surface by turbulent compositional convection. *J. Fluid Mech.* **765**, 211–228.

LIU, T. & SALAZAR, D.M. 2021 Openopticalflow_piv: an open source program integrating optical flow method with cross-correlation method for particle image velocimetry. *J. Open Res. Softw.* **9** (1).

MAGORRIAN, S.J. & WELLS, A.J. 2016 Turbulent plumes from a glacier terminus melting in a stratified ocean. *J. Geophys. Res.: Oceans* **121** (7), 4670–4696.

MALKI-EPSHTEIN, L., PHILLIPS, O.M. & HUPPERT, H.E. 2004 The growth and structure of double-diffusive cells adjacent to a cooled sidewall in a salt-stratified environment. *J. Fluid Mech.* **518**, 347–362.

MALYARENKO, A., WELLS, A.J., LANGHORNE, P.J., ROBINSON, N.J., WILLIAMS, M.J.M. & NICHOLLS, K.W. 2020 A synthesis of thermodynamic ablation at ice–ocean interfaces from theory, observations and models. *Ocean Model.* **154**, 101692.

MCCONNOCHIE, C.D. & KERR, R.C. 2016 The effect of a salinity gradient on the dissolution of a vertical ice face. *J. Fluid Mech.* **791**, 589–607.

MCCUTCHAN, A.L. & JOHNSON, B.A. 2022 Laboratory experiments on ice melting: a need for understanding dynamics at the ice–water interface. *J. Mar. Sci. Engng* **10** (8), 1008.

MORGAN, V.I. & BUDD, W.F. 1978 The distribution, movement and melt rates of Antarctic icebergs. In *Iceberg Utilization*, pp. 220–228. Elsevier.

NESHYBA, S. & JOSBERGER, E.G. 1980 On the estimation of Antarctic iceberg melt rate. *J. Phys. Oceanogr.* **10** (10), 1681–1685.

RADKO, T., FLANAGAN, J.D., STELLMACH, S. & TIMMERMANS, M.-L. 2014 Double-diffusive recipes. Part II: layer-merging events. *J. Phys. Oceanogr.* **44** (5), 1285–1305.

ROQUET, F., MADEC, G., BRODEAU, L. & NYCANDER, J. 2015 Defining a simplified yet 'realistic' equation of state for seawater. *J. Phys. Oceanogr.* **45** (10), 2564–2579.

ROSEVEAR, M.G., GAYEN, B. & GALTON-FENZI, B.K. 2021 The role of double-diffusive convection in basal melting of Antarctic ice shelves. *Proc. Natl Acad. Sci. USA* **118** (6).

SCHILD, K.M., RENSHAW, C.E., BENN, D.I., LUCKMAN, A., HAWLEY, R.L., HOW, P., TRUSEL, L., COTTIER, F.R., PRAMANIK, A. & HULTON, N.R.J. 2018 Glacier calving rates due to subglacial discharge, fjord circulation, and free convection. *J. Geophys. Res.: Earth* **123** (9), 2189–2204.

STEPHENSON, G.R., SPRINTALL, J., GILLE, S.T., VERNET, M., HELLY, J.J. & KAUFMANN, R.S. 2011 Subsurface melting of a free-floating Antarctic iceberg. *Deep-Sea Res. (*II*)* **58** (11–12), 1336–1345.

STERN, A.A., ADCROFT, A. & SERGIENKO, O. 2019 Modeling ice shelf cavities and tabular icebergs using Lagrangian elements. *J. Geophys. Res.: Oceans* **124** (5), 3378–3392.

VANCOPPENOLLE, M., MADEC, G., THOMAS, M. & MCDOUGALL, T.J. 2019 Thermodynamics of sea ice phase composition revisited. *J. Geophys. Res.: Oceans* **124** (1), 615–634.

WEADY, S., TONG, J., ZIDOVSKA, A. & RISTROPH, L. 2022 Anomalous convective flows carve pinnacles and scallops in melting ice. *Phys. Rev. Lett.* **128** (4), 044502.

WEEKS, W.F. & CAMPBELL, W.J. 1973 Icebergs as a fresh-water source: an appraisal. *J. Glaciol.* **12** (65), 207–233.

WELLS, A.J. & WORSTER, M.G. 2008 A geophysical-scale model of vertical natural convection boundary layers. *J. Fluid Mech.* **609**, 111–137.

WELLS, A.J. & WORSTER, M.G. 2011 Melting and dissolving of a vertical solid surface with laminar compositional convection. *J. Fluid Mech.* **687**, 118–140.

WILSON, N.J., VREUGDENHIL, C.A., GAYEN, B. & HESTER, E.W. 2023 Double-diffusive layer and meltwater plume effects on ice face scalloping in phase-change simulations. *Geophys. Res. Lett.* **50** (17), e2023GL104396.

WORSTER, M.G. & LEITCH, A.M. 1985 Laminar free convection in confined regions. *J. Fluid Mech.* **156**, 301–319.

YANG, R., HOWLAND, C.J., LIU, H.-R., VERZICCO, R. & LOHSE, D. 2023 Ice melting in salty water: layering and non-monotonic dependence on the mean salinity. *J. Fluid Mech.* **969**, R2.